

## Full length article

## “Self-sharpening” tungsten high-entropy alloy

Xing-Fa Liu<sup>a,b,c</sup>, Zhi-Li Tian<sup>a,b</sup>, Xian-Feng Zhang<sup>d</sup>, Hai-Hua Chen<sup>d</sup>, Tian-Wei Liu<sup>a,b,c</sup>, Yan Chen<sup>a,b,c</sup>, Yun-Jiang Wang<sup>a,b,c</sup>, Lan-Hong Dai<sup>a,b,c,\*</sup>

<sup>a</sup> State Key Laboratory of Nonlinear Mechanics, Institute of Mechanics, Chinese Academy of Sciences, Beijing 100190, China

<sup>b</sup> School of Engineering Science, University of Chinese Academy of Sciences, Beijing 101408, China

<sup>c</sup> CAS Center for Excellence in Complex System Mechanics, Beijing 100190, China

<sup>d</sup> School of Mechanical Engineering, Nanjing University of Science and Technology, Nanjing 210094, China

## ARTICLE INFO

## Article History:

Received 2 October 2019

Revised 2 January 2020

Accepted 3 January 2020

Available online 6 January 2020

## Keywords:

High-entropy alloy

Tungsten alloy

Self-sharpening

Shear band

Dynamic recrystallization

## ABSTRACT

“Self-sharpening”, a material maintaining its acute head shape during penetration, is highly desirable in a wide range of engineering applications. However, it remains a great challenge to make it occur in conventional single-principal-element alloys. Here, we develop a new chemical-disordered multi-phase tungsten high-entropy alloy that exhibits outstanding self-sharpening capability, in sharp contrast to conventional tungsten alloys only showing mushrooming. This alloy consists of a BCC dendrite phase and a rhombohedral  $\mu$  phase embedded in the continuous FCC matrix, and such a unique microstructure leads to a 10–20% better penetration performance than conventional tungsten heavy alloys. We show that emergence of the self-sharpening is triggered by the ultrastrong  $\mu$  phase stimulated dynamic recrystallization softening mediated shear banding. This study sheds light on the origin of self-sharpening and might open new opportunities for developing high-performance penetrator materials.

© 2020 Acta Materialia Inc. Published by Elsevier Ltd. All rights reserved.

## 1. Introduction

“Self-sharpening”, the capability of a material maintaining its acute head shape during penetration, is a highly required attribute of materials in armor piercing [1,2]. During penetration, the acute head reduces the resistance and thus greatly improves the efficiency of moving ahead. In anti-armor applications, tungsten heavy alloys and depleted uranium (DU) alloys are two primary families of materials. DU kinetic energy penetrators exhibit superior penetration performance due to their thermo-plastic shear banding induced “self-sharpening” behavior during penetration. While tungsten alloy kinetic energy penetrators usually form mushroom-like heads, which results in a poorer penetration performance when compared to DU alloys [2–4]. Therefore, it is needed to develop a high performance tungsten alloy to replace the DU alloy, since the DU alloys cause the environmental contamination [5]. It has been known that the self-sharpening behavior is related to localized shear deformation at high strain-rate deformation. During the past decades, substantial efforts have been put into developing new tungsten alloys with self-sharpening ability. Unfortunately, only limited success has been made [6–10]. Although the physical origin of self-sharpening still remains poorly understood, sustaining research works have shown that apart from chemical composition, the atom-packing order seems to play

an important role. Metallic glasses, known as topologically disordered alloys that fail easily by shear banding [11–14], have shown to be of high “self-sharpening” capability [15,16].

In the past few years, another new kind of disordered alloys named high-entropy alloys (HEAs), with multiple principal elements in equimolar or near-equimolar ratio, has drawn a surging interest [17–23]. The unique atomic packing, characteristic of diverse elements arranged randomly on the crystallographic positions in a topologically ordered lattice with a high chemical disorder, imparts HEA extraordinary mechanical properties, including exceptional cryogenic fracture toughness [24,25], superior performance at high temperatures [26,27], high corrosion resistance for orthopedic implants [28–30] and great potential to overcome traditional strength-ductility trade-off [31–34]. Here, one may naturally question that: could the chemical disorder in HEA promote the occurrence of “self-sharpening”? If it really does, what is the underlying mechanism? In the present study, we design a new tungsten HEA WFeNiMo with equimolar ratio to enhance chemical disorder, in contrast to conventional single-principal-element tungsten alloys, and obtain a multi-phase structured alloy. This new tungsten HEA not only possesses good combination of strength and ductility, but also excellent self-sharpening ability. In comparison with conventional single-principal-element tungsten alloys where precipitated phases are strictly suppressed, we find that the new tungsten HEA by chemical disordered design promotes precipitation of  $\mu$  phase, which can trigger dynamic recrystallization softening mediated shear banding and give rise to the prominent self-sharpening behaviors.

\* Corresponding author at: State Key Laboratory of Nonlinear Mechanics, Institute of Mechanics, Chinese Academy of Sciences, Beijing 100190, China.

E-mail address: [lhldai@lnm.imech.ac.cn](mailto:lhldai@lnm.imech.ac.cn) (L.-H. Dai).

## 2. Chemical composition design

First of all, we screened possible compositions to develop new multi-phase tungsten HEAs. Previous results have demonstrated some valuable parameters calculated from the physicochemical and thermodynamic properties of constituent alloy components can be taken into account to predict the phases formed in the equimolar multi-component alloys. Among them, atomic size difference  $\delta$  [35], the ratio of entropy to enthalpy  $\Omega$  [36], and valence electron concentration (VEC) [37] are three typical parameters to determine the phase stability for BCC or FCC solid solutions. Herein, these parameters are defined as follows, the atomic size difference

$$\delta = 100 \sqrt{\sum_{i=1}^N c_i \left( 1 - r_i / \sum_{i=1}^N c_i r_i \right)^2} \quad (1)$$

where  $c_i$  and  $r_i$  are the concentration of elements and atomic radius of the  $i$ th element, respectively.  $N$  represents the number of components in the multi-component alloy.

The thermodynamic parameter

$$\Omega = \frac{T_m \Delta S_{\text{mix}}}{|\Delta H_{\text{mix}}|} \quad (2)$$

where  $T_m$ ,  $\Delta S_{\text{mix}}$  and  $\Delta H_{\text{mix}}$  are the average melting temperature, the entropy and enthalpy of mixing of the  $n$ -element alloy, respectively, which can be calculated separately as

$$T_m = \sum_{i=1}^N c_i T_i^m \quad (2-1)$$

$$\Delta S_{\text{mix}} = -R \sum_{i=1}^N c_i \ln c_i \quad (2-2)$$

$$\Delta H_{\text{mix}} = 4 \sum_{i=1, j \neq i}^N \Delta H_{ij}^{\text{mix}} c_i c_j \quad (2-3)$$

where  $T_i^m$  being the melting point of the  $i$ th component of alloy,  $R$  is the gas constant,  $\Delta H_{ij}^{\text{mix}}$  is the enthalpy of mixing between the  $i$ th and  $j$ th component.

And valence electron concentration

$$\text{VEC} = \sum_{i=1}^n c_i (\text{VEC})_i \quad (3)$$

It has been suggested that  $\Omega \geq 1.1$  and  $\delta \leq 6.6\%$  should be used as necessary conditions for the formation of solid solution phases [36], while VEC can be utilized to predict the phase stability of FCC and BCC phases as follows [37]. Sole FCC phase exists when  $\text{VEC} \geq 8.0$ ; sole BCC phase exists when  $\text{VEC} < 6.87$ , and more than one phase

may exist when  $6.87 \leq \text{VEC} < 8.0$ . In this work, an equimolar four-component alloy WFeNiMo was chosen, with  $\delta = 4.65\%$ ,  $\Omega = 7.43$  and  $\text{VEC} = 7.5$ . According to the above empirical criterion, FCC, BCC and a third phase may coexist in this new tungsten HEA.

## 3. Materials and methods

The equimolar WFeNiMo HEA was prepared by electromagnetic levitation melting technology on a water-cooled copper crucible from raw materials with purity of 99.9% in inert atmosphere. To achieve a homogeneous distribution of constituent elements, the as-prepared alloy was re-melted four times and the alloy was kept in a liquid state for ~20 min each time. After cooling, a bulk ingot with a diameter of 60 mm and a height of 65 mm was obtained. The constituent phases of the alloy were identified by X-ray diffractometer (XRD, Rigaku Dmax 2500) using Cu K $\alpha$  target. Electron backscattered diffraction (EBSD) was conducted using a field emission scanning electron microscope (SEM, JSM-7100F) equipped with EDAX-TSL OIM EBSD system. The samples for EBSD were prepared with a Leica EM-TIC 3x ion polisher/cross sectioned using 6 kV at 2.2 mA for 12 h. The chemical composition analysis was conducted by energy-dispersive x-ray (EDX) spectroscopy on a FEI Quanta 200 SEM. Microstructures before and after deformation were also characterized by SEM and transmission electron microscope (TEM, JEM-2100F at 200 kV). The high-angle annular dark field (HAADF) image was recorded using Cs-corrected TEM, Titan Cubed G2 60–300 kV microscope with double correctors and monochromator configuration. The thin foils for TEM were first prepared by mechanical grinding to about 20–30  $\mu\text{m}$  and then polished by an iron polishing machine to achieve electron transparency. A focused ion beam (FIB) instrument (FEI Helios Nanolab 600i) was also used to accurately prepare TEM samples from deformed samples.

Nanoindentation was performed on an Agilent Nano Indenter G200 with a Berkovich diamond tip to characterize the hardness of each individual phase in WFeNiMo, with a maximum load of 5 mN at a loading rate of  $0.25 \text{ mN s}^{-1}$  and a dwell time of 10 s. Nanoindentation arrays with a spacing of 10  $\mu\text{m}$  were set [38]. SEM observations were conducted to correlate each measured value to its corresponding indent, thus ascertaining the hardness of each phase. Cylinder samples with  $\Phi 4 \times 8 \text{ mm}$  and  $\Phi 4 \times 4 \text{ mm}$  were prepared to perform the quasi-static and dynamic uniaxial compression tests, respectively. The quasi-static tests were conducted at a strain rate of  $5 \times 10^{-4} \text{ s}^{-1}$  with a MTS-810 material test system at ambient temperature. Dynamic compression tests were performed on a split Hopkinson pressure bar (SHPB) apparatus. In the SHPB experiments, the average strain rate was set to be about  $2 \times 10^3 \text{ s}^{-1}$  by controlling the impact velocity.

Penetration tests were performed using a 25 mm smooth-bore ballistic gun. The experimental layout configuration is shown in Fig. 1. A conventional tungsten alloy 93 W (W93Fe4.9Ni2.1 by weight ratio) was also examined for comparison. Blocks of both WFeNiMo and conventional 93 W were machined into rods with a dimension of  $\Phi 7 \times 50 \text{ mm}$ . To fire

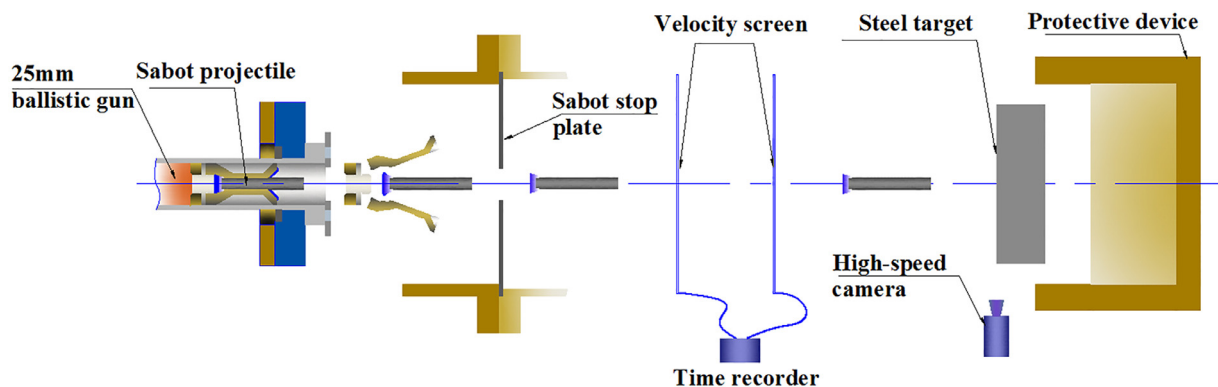
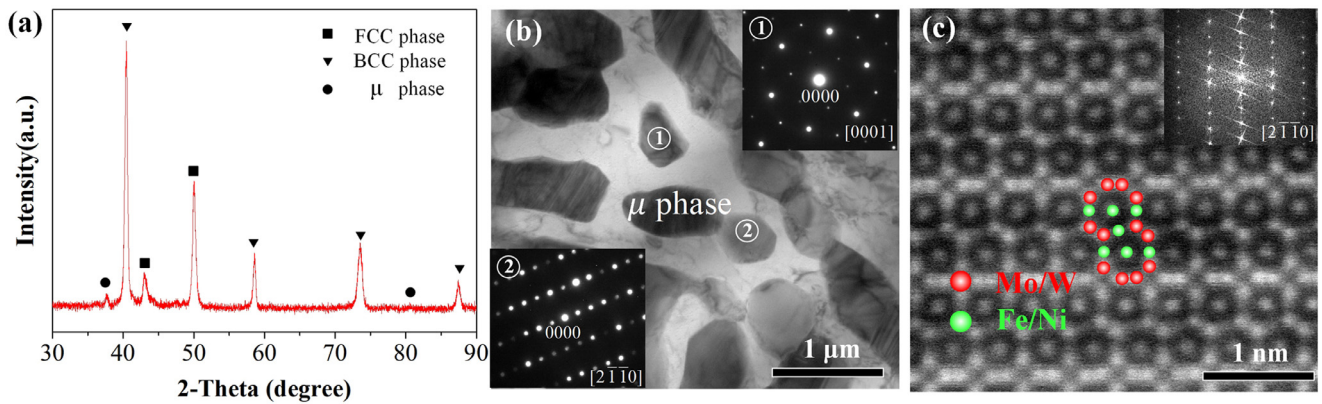


Fig. 1. Experimental layout configuration for penetration tests.



**Fig. 2.** (a) XRD pattern of as-cast WFeNiMo HEA. (b) Bright-field TEM image of the as-cast alloy, showing clustered  $\mu$  phase precipitations, with corresponding SAED patterns in the insets. (c) High-resolution HADDF/Z-contrast image of the  $\mu$  phase precipitation.

a smaller rod by the smooth bore with a larger diameter, a sabot, which consists of three separating aluminum parts and a bottom pusher, was designed and mounted at the open mouth of a cartridge. The medium carbon steel targets with 100 mm in thickness that can be considered as semi-infinite targets were placed 7 m in front of the ballistic gun. Two velocity screens and a time recorder were utilized to measure the impact velocity, which were positioned 1 m in front of the target. The impact procedures were also recorded by a high-speed camera. Projectiles were launched with velocities ranging from 876 m/s to 1330 m/s. The tests were conducted at  $0^\circ$  obliquity. After ballistic tests, targets with embedded rods were retrieved. The remnant projectiles and the targets with craters were sectioned along the symmetry plane by wire electric discharge machining to evaluate the penetration performance. The sectioned surfaces of remnants were polished to a mirror finish for further microstructural observation.

## 4. Results

### 4.1. Microstructural characterization of undeformed samples

Fig. 2(a) shows the XRD pattern of the as-cast sample. Besides the obvious peaks corresponding to FCC phase and BCC phase, there are also several small peaks indicating the existence of  $\mu$  phase precipitation. The bright-field TEM image shows clustered  $\mu$  phase precipitations with the width of about 1–2  $\mu\text{m}$ . The selected area electron diffraction (SAED) patterns that were taken along the  $[0001]$  and  $[2\bar{1}\bar{1}0]$  zone axes, as shown in the insets, confirm the  $\mu$  phase precipitations adopts a rhombohedral crystal structure. The high-angle annular dark-field (HADDF)/Z-contrast image taken along the  $[2\bar{1}\bar{1}0]$  zone axis in Fig. 2(c) further confirms the rhombohedral crystal structure of  $\mu$  phase precipitations. The Mo or W atoms overlap with the bright

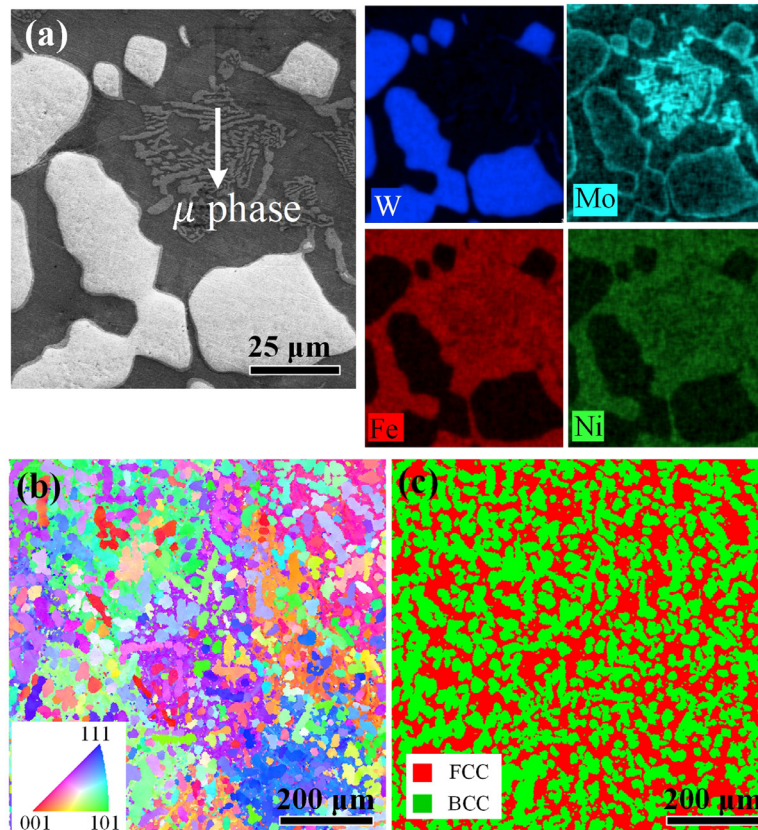


**Fig. 3.** (a) SEM image of WFeNiMo HEA and the corresponding elemental mappings. (b) EBSD IPF map and (c) phase distribution of the alloy.



**Table 1**  
Chemical composition of individual phase in WFeNiMo.

Phase	Morphology	Chemical compositions (at%)			
		W	Fe	Ni	Mo
Total	—	27.5	24.4	23.5	24.6
FCC	Continuous matrix	2.4	40.6	44.5	12.5
BCC	Dendrite	57.4	4	2	36.6
$\mu$ (Rhombohedral)	Cluster of lamellae	10.1	33.8	23	33.1

spots while Fe or Ni atoms overlap with the lower contrast spots (as will be seen in Fig. 3(a) and Table 1, all four elements are distributed in the  $\mu$  phase precipitations). These results are well matched with our intentional compositional design to obtain multi-phase structure of WFeNiMo.

The EDX analysis was conducted to examine how the constituent elements distribute in each phase. From Fig. 3(a), it can be seen that W segregates in BCC dendrites, while Fe and Ni are rich in the other two phases. Mo has a relatively homogeneous distribution among the sample. The segregation of W, Fe and Ni facilitates stabilizing the solid solution phase with a minimized Gibbs free energy. A square of  $800\ \mu\text{m} \times 800\ \mu\text{m}$  was selected to quantitatively measure the actual alloy composition, which includes substantial BCC dendrites,  $\mu$  phase precipitations and FCC matrix grains. The average chemical compositions of each phase in this alloy were calculated based on at least three independent EDX measurements, as shown in Table 1. W and Mo take up more than 90% atomic percentage in the BCC dendrites, and Fe and Ni are the main compositions in FCC matrix, while Fe and Mo are two primary elements in  $\mu$  phase. The results clearly demonstrate that, in comparison with the conventional tungsten alloy 93 W, the addition of Mo promotes the precipitation of the  $\mu$  phase [39]. Fig. 3(b) shows EBSD inverse pole figure (IPF) maps of the alloy. Typical grain sizes are 300–500  $\mu\text{m}$  for FCC matrix phase and

20–40  $\mu\text{m}$  for BCC dendrite arm diameter. No preferential orientation is observed for both FCC and BCC phases in the as-cast sample. Due to the complicated crystal structure and the small size, the precipitated  $\mu$  phase was not identified in the present EBSD result on the scale of hundreds of microns.

#### 4.2. Nano-hardness measurements and compression properties

Nanoindentations were performed to characterize the mechanical properties of each individual phase in this alloy, and the hardness and elastic modulus were measured. Due to the small size of  $\mu$  phase precipitations, as well as the limit resolution of optical microscopy installed in the measurement system, arrays with a spacing of 10  $\mu\text{m}$  were firstly set in the FCC matrix. Subsequent examinations by SEM were performed to correlate each measured value to its corresponding indent, in order to ascertain the hardness of each phase, as shown in Fig. 4(b) and (c). Fig. 4(a) shows that different phases have substantially various mechanical properties. FCC phase is the softest, with its elastic modulus similar to austenitic steels [40]. The hardness of BCC phase is nearly twice that of FCC phase, while the  $\mu$  phase achieves an extremely high hardness, up to 16.5 GPa and triples that of FCC phase.

Fig. 5 shows the compressive stress-strain curves of WFeNiMo HEA at room temperature under both quasi-static and dynamic conditions. At the strain rate of  $5 \times 10^{-4}\ \text{s}^{-1}$ , the yield strength and fracture strength are 1000 MPa and 1674 MPa, respectively, along with a fracture strain of 31%. Work hardening can be observed obviously, and the strain hardening exponent  $n$  is estimated to be 0.33, which is obtained by fitting a power law to the stress-strain curve, i.e.  $\sigma = \sigma_0 + K\varepsilon_p^n$ , where  $\sigma_0$  is the yield strength,  $K$  is the preexponential factor, and  $\varepsilon_p$  is the plastic strain. Under quasi-static compression, the strain hardening exponent of WFeNiMo HEA is smaller than that of conventional 93 W [41]. At the strain rate of  $2000\ \text{s}^{-1}$ , the yield strength, fracture strength and fracture strain are 1200 MPa,

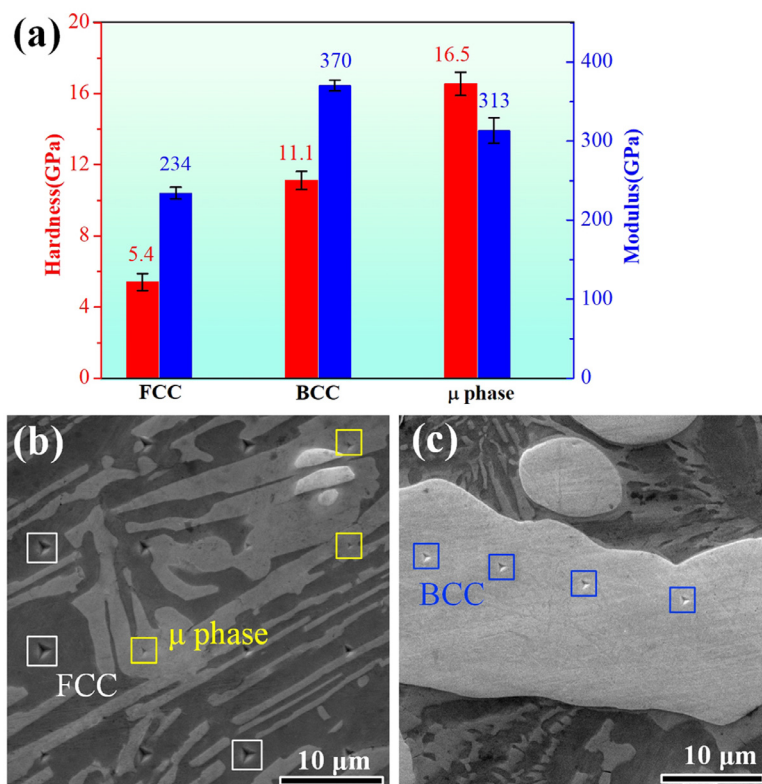


**Fig. 4.** (a) Hardness and elastic modulus of each individual phase in the nanoindentation test results for the alloy; (b) SEM images of morphology of indents in (b) the FCC matrix and (c) the BCC dendrite, with squares marking the valid indents for summarizing the statistic results for each phase.

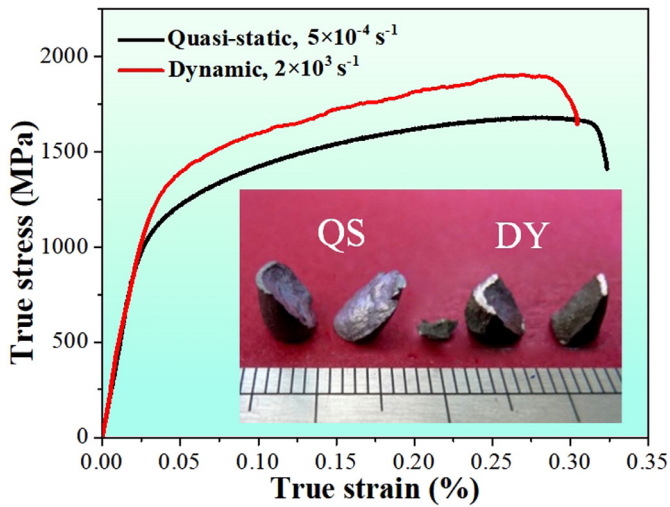


**Fig. 5.** Compressive stress–strain curves of alloy under quasi-static and dynamic conditions, with macroscopic fracture samples in the inset.

1900 MPa and 28%, respectively. Comparing these two loading conditions, the alloy exhibits strain rate hardening with the strain rate hardening exponent at the yield strength  $m = \frac{\Delta \log \sigma}{\Delta \log \dot{\epsilon}}$  estimated to be 0.012, where  $\sigma$  is the yield stress and  $\dot{\epsilon}$  is the strain rate. This value is smaller than that of conventional 93 W, 0.042 [41], indicating that WFeNiMo HEA is less sensitive to strain rate. It is worth noting that the alloy fractures in a shear mode, indicative of the potential to demonstrate “self-sharpening” behavior.

Microstructures of the deformed samples were examined by TEM to understand the deformation mechanisms and the reason for the

good combination of strength and plasticity of this new tungsten HEA. Fig. 6(a)–(c) show the TEM bright-field images of each phase in the sample upon dynamic loadings. The complex stress state inflicted on the BCC dendrites activated multiply slip systems in it. The deformed BCC phase is characteristic of high-density tangled dislocations without twins, which demonstrates a certain amount of plastic deformation of W-Mo-rich BCC phase. As indicated from Fig. 6(b), dislocations in FCC matrix pile up near the boundary between  $\mu$  phase and FCC phase. The  $\mu$  phase precipitation was not plastically sheared, and acted as blocks for dislocation motions in FCC. Fig. 6(c) shows parallel nanotwins with thickness of 10 ~ 30 nm formed in FCC during deformation, confirmed by the twinning spots in the SAED pattern and the high-resolution TEM (HRTEM) image. Not only do these nanotwins provided plasticity, but also offered effective obstacles to the motion of dislocations (indicated in Fig. 6(d)) and gave rise to work hardening for continuous straining [42,43].

#### 4.3. Ballistic performance

The penetration performance of the alloy under high-speed impact was further investigated through ballistic experiments. Rods made of a typical conventional tungsten alloy 93 W were also examined for comparison. Fig. 7(a) shows the curves of DOP versus kinetic energy per volume calculated by  $\rho v^2/2$ , where  $\rho$  is density, and  $v$  is impact velocity. The density was measured using Archimedeian principle, with the results 12.7 g/cm<sup>3</sup> for WFeNiMo and 17.5 g/cm<sup>3</sup> for 93 W. In general, the relationship between DOP and kinetic energy is approximately linear for both alloys, but this new alloy performs better and it achieves 10–20% larger penetration depth than 93 W at the same imposed kinetic energy. From the inset in Fig. 7(a) of the retrieved remnants, it can be observed that the remnant of 93 W penetrator has suffered severe plastic deformation and exhibits an

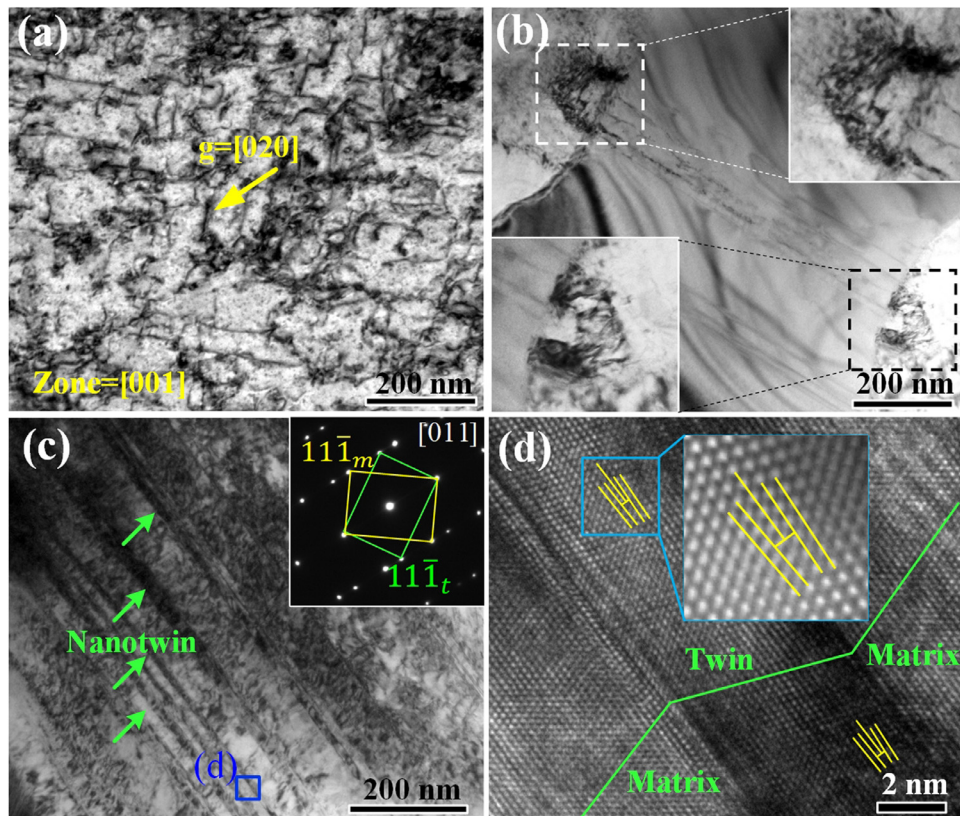


**Fig. 6.** Bright-field TEM images of each phase in deformed WFeNiMo HEA: (a) dislocation tangles formed in BCC phase, (b) block of dislocations in FCC matrix near the  $\mu$  phase precipitation, (c) deformation nanotwins with a thickness of 10–30 nm and the SAED pattern in the inset, (d) HRTEM image of the region marked in (c).



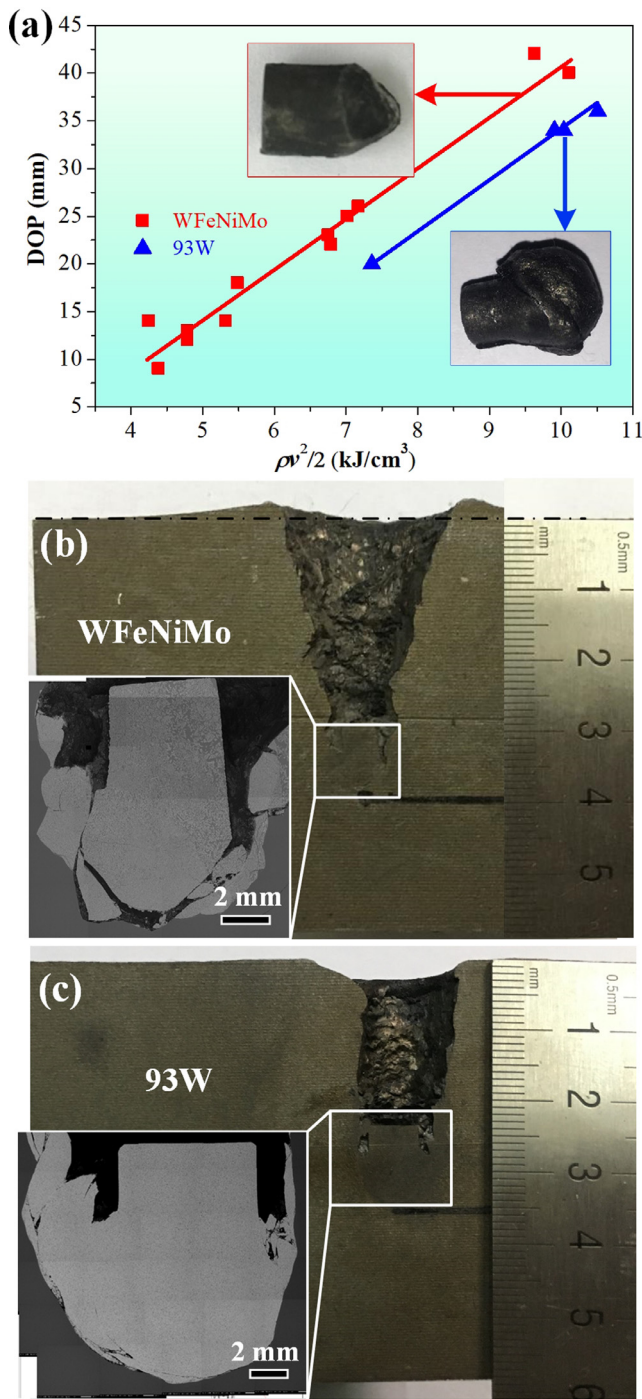


**Fig. 7.** (a) Depth of penetration of WFeNiMo rod and 93 W rod versus kinetic energy per volume calculated by  $\rho v^2/2$ , with photographs of the retrieved remnants, respectively; longitudinal sections of medium carbon steel targets impacted by (b) a WFeNiMo penetrator and (c) a 93 W penetrator, with SEM micrographs of the remnant in the corresponding insets, respectively.

obvious mushroom-like head. In contrast, the remnant of WFeNiMo penetrator maintains an acute head shape, demonstrating a conspicuous self-sharpening ability, which is responsible for the improved penetration performance of WFeNiMo penetrators.

Fig. 7(b) and (c) shows typical sectioned targets along with a residual WFeNiMo penetrator and a residual 93 W penetrator, respectively. The penetration tunnel on the target for WFeNiMo HEA is a trumpet-like shape, and the wall is coarse due to the debris separated from the rod. At the end of bottom, the remnant rod maintains an acute head, with fragments falling off the main body along the

direction about  $45^\circ$  to the impact direction. For the 93 W, an obvious mushroom-like remnant can be seen, and the penetration tunnel is circular with its width nearly twice of the initial diameter of 93 W rod. As the plastic flow was relatively stable, the eroded mass that flowed reversely along the lateral edge led to a smoother wall than that of the target impacted by WFeNiMo.

#### 4.4. Microstructure analysis on the remnant

A closer examination on the remnant by SEM was conducted to investigate the details of “self-sharpening” behavior of WFeNiMo penetrator. In the fragment (Fig. 8(a)), it is clear to see a shear band near the edge. Along its propagation from top left to bottom right, the shear band becomes thicker, and finally turns into a crack with voids formation there, resembling the morphology of shear bands in the shock-loaded TC4 alloy [44], low-carbon steels [45], and U-2Mo alloy [46]. Fig. 8(b) and (c) shows the deformed microstructure of the main body. Near the edge, BCC dendrites were sheared and got a fibrous tail approximately  $25^\circ$ – $45^\circ$  inclined to the impact direction, indicating severe plastic deformation. The shear band propagated into the inner region, narrowed down to several micrometers and cut BCC dendrites into halves. These readily observed localized shear deformation behaviors suggest the self-sharpening ability of WFeNiMo mainly results from its relatively high susceptibility to shear banding.

To study microstructural features of shear bands, TEM foil samples were prepared by focus ion beam (FIB) milling technique from areas perpendicular to shear bands, marked by the yellow rectangles in the insets of Fig. 8(b) and (c). Fig. 9 demonstrates the details of the shear localized region indicated in the inset of Fig. 8(b), and the arrows in the figures indicate the same view direction. This specimen includes  $\mu$  phase particles and FCC matrix. The  $\mu$  phase particles appear non-deformable, as indicated from Fig. 6(b). In the FCC matrix, two distinct regions are distinguished by different features: the elongated lath subgrains and the relatively fine rectangular or equiaxed subgrains. Fine equiaxed subgrains with various crystalline orientations are mainly located near the  $\mu$  phase particles (Fig. 9(b) and (d)), indicated by the SAED patterns with stretched spots and partial rings. While between location b and d, there appear elongated lath subgrains situated relatively far from the particles (Fig. 9(c)). In this region, these subgrains have a narrow width of 50–80 nm and the aspect ratio (length/width) is often more than 10. The relatively straight boundaries between them are clearly observed and roughly parallel to the shear direction. The SAED pattern here exhibits discrete elongated spots but clearly displays a  $[110]$  zone axis. In addition to the alternating black and white regions with high contrast, the diffraction pattern indicates the laths subgrains have misorientations between each other, yet still retain some crystalline characteristics of the FCC matrix. When approaching the  $\mu$  phase particles, the subgrains maintained a width similar to that of the elongated lath subgrains but their lengths were reduced to a rectangular shape, even equiaxed state adjacent to the particles. Noting that the rectangular subgrains, mixed with equiaxed subgrains, demonstrate boundaries along the shear direction, it suggests a linkage between the equiaxed subgrains and the elongated parent subgrains. A mechanism involving two main processes, namely the splitting and breakdown, has been proposed to delineate the transition from the elongated substructure to the fine subgrains within the shear band [47,48]. The splitting, driven by the shear stress along the shear direction, results in thinner lath subgrains. While the conjugated shear stress offers the powerhouse to break down the elongated lath substructures into pieces with a reduced aspect ratio in the transverse direction. The breakdown process provides evidence that the fine subgrains strongly correlate with the original substructure before the formation of shear localization. Furthermore, such a solid linkage, associated with the blurred subgrain boundaries of the fine subgrains, implies that the grain refinement cannot be a result of conventional dynamic recrystallization

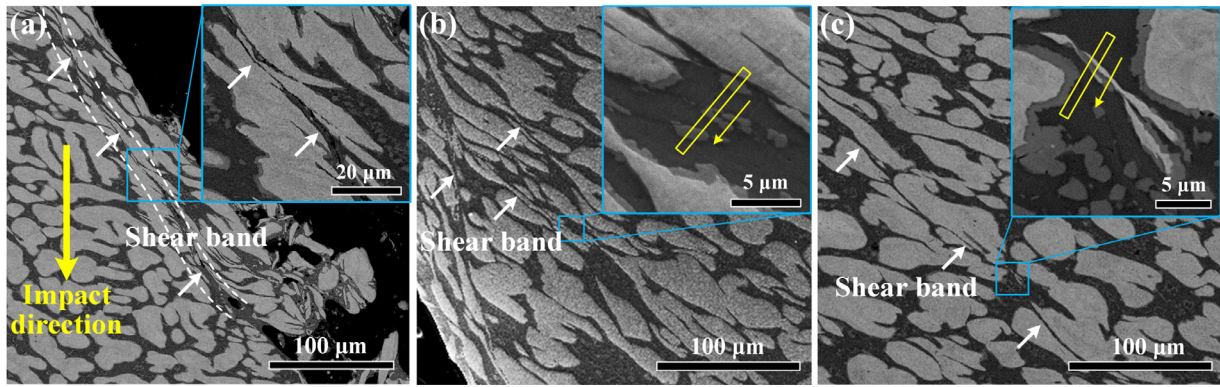


**Fig. 8.** Magnified SEM images of regions near the fracture surface of WFeNiMo remnant in the inset of Fig. 7(b), showing shear bands formation in (a) the debris, (b) and (c) the main body. The yellow rectangles in the insets of (b) and (c) mark the regions for FIB milling to prepare TEM foils.

(DRX), which includes distinct nucleation and growth of new grains [49]. The current observation of nanocrystals in the shear band is suggestive of a rotational dynamic recrystallization mechanism [50–53].

The montage in Fig. 10 shows the microstructure of a well-developed shear band marked in Fig. 8(c), from the center to its boundary. This montage covers all the three phases, and various substructures can be observed. For BCC phase located on the left of Fig. 10, the grain splitted into several elongated lath subgrains with the long axis parallel to the shear direction. The split spots in the corresponding diffraction pattern suggests the misorientation between lath subgrains. While for the FCC phase, there exists a gradient substructure with size of tens of nanometers in the center gradually increasing to several microns at the edge. The gradually increasing dimension of substructure from the center to the boundary usually manifests the

decreasing shear strain. In the core of the shear band, these equiaxed subgrains possess a range of dimensions varying from 30 to 80 nm, which are smaller than those of Fig. 9 and indicates a larger shear strain. The almost continuous diffraction ring pattern implies these equiaxed subgrains are randomly distributed with no preferential orientation, signifying severe grain refinement. When approaching to the boundary of the shear band, the FCC phase changed to elongated subgrains, similar to the characteristics of BCC phase. At the edge of the shear band, thick dislocation walls along the shear direction and dislocation tangles are observed in the FCC grains. The transition from the micro sized FCC grain to the extremely refined subgrain indicates the occurrence of rotational DRX in the shear band. The  $\mu$  phase particles, adjacent to the ultrafine subgrains of the FCC phase, deformed much less and approximated rigid during the deformation.

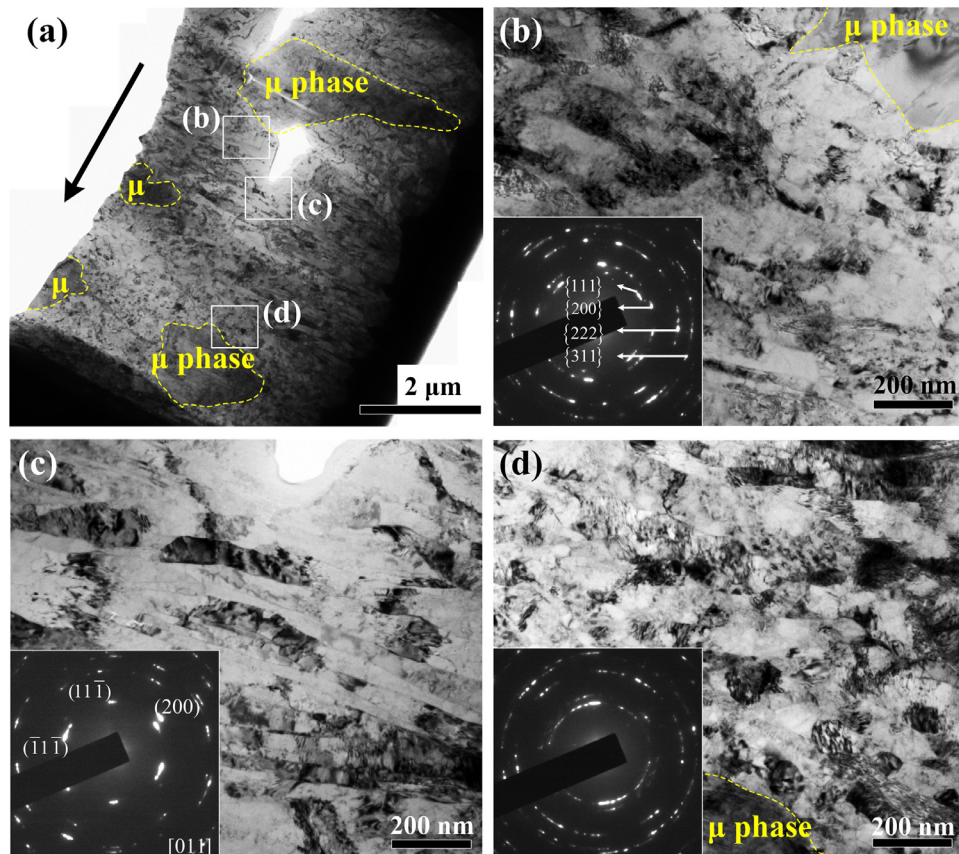


**Fig. 9.** Microstructures of the shear band in the inset of Fig. 8(b): (a) low magnification bright-field TEM image of the shear band; (b)–(d) magnified images of the regions marked b, c, d in (a) with insets the corresponding SAED patterns, respectively.



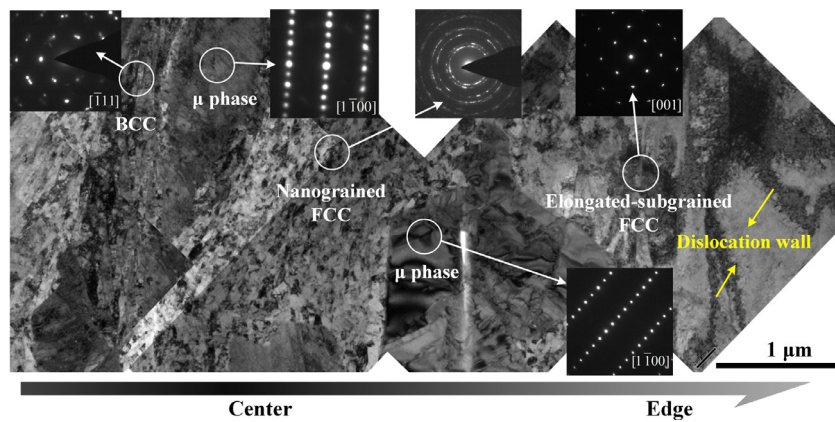


Fig. 10. Bright-field TEM image of the microstructure of the shear band in inset of Fig. 8(c) from the center to its edge.

It is worth noting that the nanosized DRX grain region associated with the largest deformation in the center are sandwiched by  $\mu$  phase precipitations, which suggests that the ultrahard  $\mu$  phase particles may play an important role in the grain refinement of FCC phase and the resultant formation of the shear band.

## 5. Discussion

Previous studies on HEA have shown that dual-phase or multi-phase HEAs may take advantage of their heterophase nature to achieve superior mechanical attributes [34,54,55]. The present multi-phase WFeNiMo alloy consists of FCC, BCC and a precipitation phase. It exhibits a good combination of high fracture strength ( $\sim 1.9$  GPa) and considerable ductility (fracture strain  $\sim 28\%$ ) under dynamic condition. In comparison with a pure FCC solid solution such as CoCrFeMnNi, the strength is greatly elevated. Similar to dual-phase steels [56] or particle reinforced metal matrix composites [57], the presence of stronger and stiffer phases, as BCC dendrites and  $\mu$  phase in the present alloy, brings about load transfer from the FCC matrix. Since they totally take up over 55% of the volume fraction, they carry a high proportion of the externally applied load, resulting in higher strength. As deformation continues, the elastic-plastic mismatch will induce plastic strain gradient at the interfaces, associated with the formation of geometrically necessary dislocations (GNDs) and the impeding effect on dislocation motion [58,59]. In the present alloy, the densely distributed  $\mu$  phase precipitations as well as their relatively small size in the FCC matrix can cause a great increase of dislocation density (Fig. 6(b)) and give rise to a further strengthening effect. Furthermore, solid solution strengthening, forest dislocation strengthening and mechanical twinning of the FCC matrix can lead to a high strain hardening ability and promote the compressive ductility [60,61].

Previous reports on the penetration behaviors of depleted uranium alloys [2,3] and tungsten fiber reinforced metallic glass composites [15,16] attribute the self-sharpening ability to their high susceptibility to shear band formation during penetration. From the shear failure mode in dynamic compression as well as the microscopic morphology of the remnant of WFeNiMo penetrator, we suggest that this alloy achieves “self-sharpening” behavior due to that the unique structure makes it more susceptible to shear band formation. During penetration, shear bands formed at the edge of WFeNiMo penetrator heads. Thus deformed parts fell off easily along these shear bands, which made the penetrator rods remain an acute shape (Figs. 7 and 8). In contrast, conventional tungsten alloys like 93 W as a comparison in the present study, demonstrate stable plastic flows and form mushroomed heads. As is known, a shear band usually tends to nucleate when softening mechanisms overcome all other hardening effects. Many experimental results have shown that dynamic recrystallization (DRX) takes place inside the shear bands for a large number of alloys [44,51–53,62].

Recently, DRX has been regarded as a potential physical origin for shear band formation [62–64], as the occurrence of DRX is accompanied by a sudden reduction of dislocation density that finally leads to an instant stress drop [49]. To drive DRX softening occurrence, there should be enough stored energy that mainly manifests as high-density dislocations. It has been known that in materials with heterophase structure dislocations usually pile up at structural inhomogeneity sites such as reinforced particles or precipitations dispersed in the matrix. As a result of different mechanical properties between the particles and the matrix, the deformation incompatibility lead to strain gradients at the interface [59,65]. In our previous researches on SiC particle reinforced aluminum composites, we showed that smaller particles induce a higher strain gradient which makes the composites more susceptible to shear band formation [66,67]. In the present study, the addition of Mo and the equimolar ration of constituent elements, in comparison with 93 W, increased the chemical disorder of WFeNiMo and promoted the precipitations of  $\mu$  phase (Fig. 2). The micronized  $\mu$  phase precipitations, which are absent in 93 W, are non-deformable and serve as the role similar to the small reinforced particles in metal matrix composites that promote the formation of shear bands. To accommodate the elastic–plastic mismatch between the constituent phases during deformation, GNDs were generated and stored near the phase boundaries, and then blocked the slip of mobile dislocations in FCC matrix on the primary slip plane together with the  $\mu$  phase precipitations. This greatly increased the dislocation density and thus enough stored energy to drive recrystallization [62,68]. This may be the reason for that the FCC phase sandwiched by  $\mu$  phase precipitations becomes recrystallized nanograins in the core of the shear band (Fig. 10). Meanwhile, strain partition took place because each phase has different mechanical properties (Fig. 4). Being the softest, the continuous FCC matrix sustained the largest part of plastic strain, similar to what the FCC phase did in dual-phase  $\text{Al}_{0.5}\text{CoCrFeNi}$  revealed by digital image correlation [55]. In order to allow for the high strain at the very high strain rate during penetration, the FCC grains were divided into elongated subgrains that then broke or rotated into approximately equiaxed nanograins, namely the rotational DRX [48,52,53]. A schematic drawing showing the shear localization process and the effect of  $\mu$  phase precipitations is presented in Fig. 11(a)–(e). It can be clearly seen that the  $\mu$  phase precipitations dispersed in FCC matrix give rise to a more inhomogeneous deformation and cause relatively higher strain gradients, which thus stimulates DRX and leads to shear band formation. This is the main reason for the self-sharpening ability of WFeNiMo penetrators. Previous studies on shear banding in particle reinforced metal matrix composites [57,59,66,67] and metallic glasses [69,70] also confirmed that the presence of a high level of micro/nano-scale structural heterogeneities induces large strain gradients, which in turn enhances the susceptibility of shear banding. Overall,  $\mu$  phase precipitations play the key role in promoting the formation of shear bands and the resultant “self-sharpening” behavior.



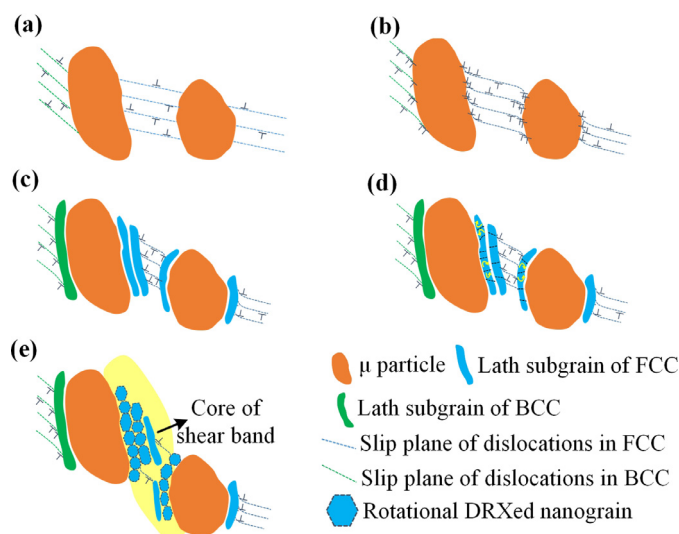


**Fig. 11.** Schematic drawing showing the shear localization mechanism for WFeNiMo HEA. (a) initial microstructure with low dislocation density before deformation; (b) formation of strain gradient due to geometrically necessary dislocations (GNDs) being generated and stored near the phase boundaries to accommodate elastic-plastic mismatch between the constituent phases; (c) dislocation continuous accumulation and formation of elongated lath subgrains to accommodate deformation; (d) elongated lath subgrains of FCC subdivided into equiaxed subgrains and rotated to accommodate further deformation; (e) formation of highly misoriented grains and equiaxed grains, accompanied with a reduction of dislocation density and the occurrence of a shear band.

## 6. Conclusions

In this study, we design a new multi-phase tungsten HEA that exhibits extraordinary self-sharpening ability. This tungsten HEA, characteristic of a dendrite BCC phase and a rhombohedral  $\mu$  phase precipitation embedded in the continuous FCC matrix, obtains excellent strength (1.9 GPa) and ductility (28%) under dynamic compression. Our results demonstrate that the multi-phase structure, especially the presence of micronized ultrastrong  $\mu$  phase precipitations, promotes an inhomogeneous deformation and causes a large strain gradient between the precipitations and FCC matrix. During penetration, the stored energy manifested as high-density dislocations associated with the strain gradient, drives dynamic recrystallization softening that contributes to the formation of shear bands and the resultant self-sharpening behavior. To our knowledge, this work constitutes the first report of penetration performance of tungsten HEAs. Our study may pave the way for developing new high-performance penetrator materials.

## Declaration of competing interest

None.

## Acknowledgments

This work is financially supported by the NSFC (Nos. 11790292, 51901235), the National Key Research and Development Program of China (No. 2017YFB0702003), the Strategic Priority Research Program (Nos. XDB22040302 and XDB22040303), the Key Research Program of Frontier Sciences (Grant No. QYZDJSSW-JSC011), and the Youth Promotion Association of Chinese Academy of Sciences.

## References

- [1] W.D. Cai, Y. Li, R.J. Dowding, F.A. Mohamed, E.J. Lavarnia, A review of tungsten-based alloys as kinetic energy penetrator materials, *Rev. Particulate Mater.* 3 (1995) 71–131.
- [2] M.A. Meyers, *Dynamic Behavior of Materials*, John Wiley, New York, 1994.
- [3] L.S. Magness, High strain rate deformation behaviors of kinetic energy penetrator materials during ballistic impact, *Mech. Mater.* 17 (2) (1994) 147–154.
- [4] D.-K. Kim, S. Lee, W. Hyung Baek, Microstructural study of adiabatic shear bands formed by high-speed impact in a tungsten heavy alloy penetrator, *Mater. Sci. Eng., A* 249 (1) (1998) 197–205.
- [5] D.P. Arfsten, K.R. Still, G.D. Ritchie, A review of the effects of uranium and depleted uranium exposure on reproduction and fetal development, *Toxicol. Ind. Health* 17 (5–10) (2001) 180–191.
- [6] R. Dandliker, R. Conner, W. Johnson, Melt infiltration casting of bulk metallic-glass matrix composites, *J. Mater. Res.* 13 (10) (1998) 2896–2901.
- [7] A. Upadhyaya, Processing strategy for consolidating tungsten heavy alloys for ordnance applications, *Mater. Chem. Phys.* 67 (1) (2001) 101–110.
- [8] Q. Wei, T. Jiao, K.T. Ramesh, E. Ma, L.J. Kecskes, L. Magness, R. Dowding, V.U. Kazykhanov, R.Z. Valiev, Mechanical behavior and dynamic failure of high-strength ultrafine grained tungsten under uniaxial compression, *Acta Mater.* 54 (1) (2006) 77–87.
- [9] X. Zhou, S. Li, J. Liu, Y. Wang, X. Wang, Self-sharpening behavior during ballistic impact of the tungsten heavy alloy rod penetrators processed by hot-hydrostatic extrusion and hot torsion, *Mater. Sci. Eng. A* 527 (18–19) (2010) 4881–4886.
- [10] R. Luo, D. Huang, M. Yang, E. Tang, M. Wang, L. He, Penetrating performance and “self-sharpening” behavior of fine-grained tungsten heavy alloy rod penetrators, *Mater. Sci. Eng. A* 675 (2016) 262–270.
- [11] L.H. Dai, Y.L. Bai, Basic mechanical behaviors and mechanics of shear banding in BMGs, *Int. J. Impact Eng.* 35 (8) (2008) 704–716.
- [12] A.L. Greer, Y.Q. Cheng, E. Ma, Shear bands in metallic glasses, *Mater. Sci. Eng. R* 74 (4) (2013) 71–132.
- [13] C. Schuh, T. Huftnagel, U. Ramamurty, Mechanical behavior of amorphous alloys, *Acta Mater.* 55 (12) (2007) 4067–4109.
- [14] D. Rodney, A. Tanguy, D. Vandembroucq, Modeling the mechanics of amorphous solids at different length scale and time scale, *Modell. Simul. Mater. Sci. Eng.* 19 (8) (2011) 083001.
- [15] R.D. Conner, R.B. Dandliker, V. Scruggs, W.L. Johnson, Dynamic deformation behavior of tungsten-fiber/metallic-glass matrix composites, *Int. J. Impact Eng.* 24 (5) (2000) 435–444.
- [16] X.W. Chen, L.M. Wei, J.C. Li, Experimental research on the long rod penetration of tungsten-fiber/Zr-based metallic glass matrix composite into Q235 steel target, *Int. J. Impact Eng.* 79 (2015) 102–116.
- [17] J.W. Yeh, S.K. Chen, S.J. Lin, J.Y. Gan, T.S. Chin, T.T. Shun, C.H. Tsau, S.Y. Chang, Nanostructured high-entropy alloys with multiple principal elements: novel alloy design concepts and outcomes, *Adv. Eng. Mater.* 6 (5) (2004) 299–303.
- [18] B. Cantor, I.T.H. Chang, P. Knight, A.J.B. Vincent, Microstructural development in equiatomic multicomponent alloys, *Mater. Sci. Eng., A* 375–377 (2004) 213–218.
- [19] Y. Zhang, T.T. Zuo, Z. Tang, M.C. Gao, K.A. Dahmen, P.K. Liaw, Z.P. Lu, Microstructures and properties of high-entropy alloys, *Prog. Mater. Sci.* 61 (2014) 1–93.
- [20] D.B. Miracle, O.N. Senkov, A critical review of high entropy alloys and related concepts, *Acta Mater.* 122 (2017) 448–511.
- [21] Z. Li, S. Zhao, R.O. Ritchie, M.A. Meyers, Mechanical properties of high-entropy alloys with emphasis on face-centered cubic alloys, *Prog. Mater. Sci.* 102 (2019) 296–345.
- [22] E.P. George, D. Raabe, R.O. Ritchie, High-entropy alloys, *Nat. Rev. Mater.* 4 (2019) 515–534.
- [23] Y.F. Ye, Q. Wang, J. Lu, C.T. Liu, Y. Yang, High-entropy alloy: challenges and prospects, *Mater. Today* 19 (6) (2016) 349–362.
- [24] B. Gludovatz, A. Hohenwarter, D. Catoor, E.H. Chang, E.P. George, R.O. Ritchie, A fracture-resistant high-entropy alloy for cryogenic applications, *Science* 345 (6201) (2014) 1153–1158.
- [25] F. Otto, A. Dlouhý, C. Somsen, H. Bei, G. Eggeler, E.P. George, The influences of temperature and microstructure on the tensile properties of a CoCrFeMnNi high-entropy alloy, *Acta Mater.* 61 (15) (2013) 5743–5755.
- [26] O.N. Senkov, G.B. Wilks, J.M. Scott, D.B. Miracle, Mechanical properties of Nb25Mo25Ta25W25 and V20Nb20Mo20Ta20W20 refractory high entropy alloys, *Intermetallics* 19 (5) (2011) 698–706.
- [27] O.N. Senkov, S. Gorsse, D.B. Miracle, High temperature strength of refractory complex concentrated alloys, *Acta Mater.* 175 (2019) 394–405.
- [28] S.P. Wang, J. Xu, TiZrNbTaMo high-entropy alloy designed for orthopedic implants: as-cast microstructure and mechanical properties, *Mater. Sci. Eng., C* 73 (2017) 80–89.
- [29] S.P. Wang, J. Xu, (TiZrNbTa)-Mo high-entropy alloys: dependence of microstructure and mechanical properties on Mo concentration and modeling of solid solution strengthening, *Intermetallics* 95 (2018) 59–72.
- [30] Z. Guo, X. Pang, Y. Yan, K. Gao, A.A. Volinsky, T.Y. Zhang, CoCrMo alloy for orthopedic implant application enhanced corrosion and tribocorrosion properties by nitrogen ion implantation, *Appl. Surf. Sci.* 347 (2015) 23–34.
- [31] J.Y. He, H. Wang, H.L. Huang, X.D. Xu, M.W. Chen, Y. Wu, X.J. Liu, T.G. Nieh, K. An, Z.P. Lu, A precipitation-hardened high-entropy alloy with outstanding tensile properties, *Acta Mater.* 102 (2016) 187–196.
- [32] T. Yang, Y.L. Zhao, Y. Tong, Z.B. Jiao, J. Wei, J.X. Cai, X.D. Han, D. Chen, A. Hu, J.J. Kai, K. Lu, Y. Liu, C.T. Liu, Multicomponent intermetallic nanoparticles and superb mechanical behaviors of complex alloys, *Science* 362 (6417) (2018) 933–937.
- [33] Z.F. Lei, X.J. Liu, Y. Wu, H. Wang, S.H. Jiang, S.D. Wang, X.D. Hui, Y.D. Wu, B. Gault, P. Kontis, D. Raabe, L. Gu, Q.H. Zhang, H.W. Chen, H.T. Wang, J.B. Liu, K. An, Q.S. Zeng, T.G. Nieh, Z.P. Lu, Enhanced strength and ductility in a high-entropy alloy via ordered oxygen complexes, *Nature* 563 (7732) (2018) 546–550.
- [34] Z. Li, K.G. Pradeep, Y. Deng, D. Raabe, C.C. Tasan, Metastable high-entropy dual-phase alloys overcome the strength-ductility trade-off, *Nature* 534 (7606) (2016) 227–230.

- [35] Y. Zhang, Y.J. Zhou, J.P. Lin, G.L. Chen, P.K. Liaw, Solid-solution phase formation rules for multi-component alloys, *Adv. Eng. Mater.* 10 (6) (2008) 534–538.
- [36] X. Yang, Y. Zhang, Prediction of high-entropy stabilized solid-solution in multi-component alloys, *Mater. Chem. Phys.* 132 (2) (2012) 233–238.
- [37] S. Guo, C. Ng, J. Lu, C.T. Liu, Effect of valence electron concentration on stability of fcc or bcc phase in high entropy alloys, *J. Appl. Phys.* 109 (10) (2011).
- [38] R. Maaß, P. Birckigt, C. Borchers, K. Samwer, C.A. Volkert, Long range stress fields and cavitation along a shear band in a metallic glass: the local origin of fracture, *Acta Mater.* 98 (2015) 94–102.
- [39] A. Bose, R.M. German, Matrix composition effects on the tensile properties of tungsten-molybdenum heavy alloys, *Metall. Trans. A* 21 (4) (1990) 1325–1327.
- [40] D. Gerlich, S. Hart, Pressure dependence of the elastic moduli of three austenitic stainless steels, *J. Appl. Phys.* 55 (4) (1984) 880–884.
- [41] Z. Xu, F. Huang, Thermomechanical behavior and constitutive modeling of tungsten-based composite over wide temperature and strain rate ranges, *Int. J. Plast.* 40 (2013) 163–184.
- [42] Q. Lu, Z. You, X. Huang, N. Hansen, L. Lu, Dependence of dislocation structure on orientation and slip systems in highly oriented nanotwinned Cu, *Acta Mater.* 127 (2017) 85–97.
- [43] L. Lu, X. Chen, X. Huang, K. Lu, Revealing the maximum strength in nanotwinned copper, *Science* 323 (5914) (2009) 607.
- [44] H.A. Grebe, H.-R. Pak, M.A. Meyers, Adiabatic shear localization in titanium and Ti-6 pct Al-4 pct V alloy, *Metall. Trans. A* 16 (5) (1985) 761–775.
- [45] M.A. Meyers, C.L. Wittman, Effect of metallurgical parameters on shear band formation in low-carbon (~0.20 wt pct) steels, *Metall. Trans. A* 21 (12) (1990) 3153–3164.
- [46] C.D.R. Board, C.D.o.N. Defence, C.d.r.p.I.d. Valcartier, C.d.r.p.I. defense, D.R.E. Valcartier, G. Irwin, Metallographic interpretation of impacted ogive penetrators, Defence Research Board (1972).
- [47] Q. Xue, G.T. Gray, Development of adiabatic shear bands in annealed 316 L stainless steel: part II. TEM studies of the evolution of microstructure during deformation localization, *Metall. Mater. Trans. A* 37 (8) (2006) 2447–2458.
- [48] M.A. Meyers, Y.B. Xu, Q. Xue, M.T. Perez-Prado, T.R. McNelley, Microstructural evolution in adiabatic shear localization in stainless steel, *Acta Mater.* 51 (5) (2003) 1307–1325.
- [49] T. Sakai, A. Belyakov, R. Kaibyshev, H. Miura, J.J. Jonas, Dynamic and post-dynamic recrystallization under hot, cold and severe plastic deformation conditions, *Prog. Mater. Sci.* 60 (2014) 130–207.
- [50] M.A. Meyers, H.R. Pak, Observation of an adiabatic shear band in titanium by high-voltage transmission electron microscopy, *Acta Metall.* 34 (12) (1986) 2493–2499.
- [51] J.A. Hines, K.S. Vecchio, Recrystallization kinetics within adiabatic shear bands, *Acta Mater.* 45 (2) (1997) 635–649.
- [52] Z. Li, S. Zhao, B. Wang, S. Cui, R. Chen, R.Z. Valiev, et al. The effects of ultra-fine-grained structure and cryogenic temperature on adiabatic shear localization in titanium, *Acta Mater.* (2019).
- [53] Q. Xue, E.K. Cerreta, G.T. Gray III, Microstructural characteristics of post-shear localization in cold-rolled 316 L stainless steel, *Acta Mater.* 55 (2) (2007) 691–704.
- [54] W.H. Liu, Z.P. Lu, J.Y. He, J.H. Luan, Z.J. Wang, B. Liu, Y. Liu, M.W. Chen, C.T. Liu, Ductile CoCrFeNiMo<sub>x</sub> high entropy alloys strengthened by hard intermetallic phases, *Acta Mater.* 116 (2016) 332–342.
- [55] M. Bonisch, Y. Wu, H. Sehitoglu, Twinning-induced strain hardening in dual-phase FeCoCrNiAl<sub>0.5</sub> at room and cryogenic temperature, *Sci. Rep.* 8 (1) (2018) 10663–10663.
- [56] H. Ghassemi-Armaki, R. Maaß, S.P. Bhat, S. Sriram, J.R. Greer, K.S. Kumar, Deformation response of ferrite and martensite in a dual-phase steel, *Acta Mater.* 62 (2014) 197–211.
- [57] L.H. Dai, Z. Ling, Y.L. Bai, Size-dependent inelastic behavior of particle-reinforced metal-matrix composites, *Compos. Sci. Technol.* 61 (8) (2001) 1057–1063.
- [58] M.F. Ashby, The deformation of plastically non-homogeneous materials, *Phil. Mag.* 21 (170) (1970) 399–424.
- [59] L.H. Dai, Z. Ling, Y.L. Bai, A strain gradient-strengthening law for particle reinforced metal matrix composites, *Scr. Mater.* 41 (3) (1999) 245–251.
- [60] Z. Li, S. Zhao, H. Diao, P. Liaw, M. Meyers, High-velocity deformation of Al 0. 3 CoCrFeNi high-entropy alloy: remarkable resistance to shear failure, *Sci. Rep.* 7 (2017) 42742.
- [61] S.W. Wu, G. Wang, Q. Wang, Y.D. Jia, J. Yi, Q.J. Zhai, et al. Enhancement of strength-ductility trade-off in a high-entropy alloy through a heterogeneous structure, *Acta Mater.* 165 (2019) 444–458.
- [62] D. Rittel, P. Landau, A. Venkert, Dynamic recrystallization as a potential cause for adiabatic shear failure, *Phys. Rev. Lett.* 101 (16) (2008) 165501.
- [63] S.N. Medyanik, W.K. Liu, S. Li, On criteria for dynamic adiabatic shear band propagation, *J. Mech. Phys. Solids* 55 (7) (2007) 1439–1461.
- [64] J.A. Rodríguez-Martínez, G. Vadillo, D. Rittel, R. Zaera, J. Fernández-Sáez, Dynamic recrystallization and adiabatic shear localization, *Mech. Mater.* 81 (2015) 41–55.
- [65] Z. Xue, Y. Huang, M. Li, Particle size effect in metallic materials: a study by the theory of mechanism-based strain gradient plasticity, *Acta Mater.* 50 (1) (2002) 149–160.
- [66] L.H. Dai, L.F. Liu, Y.L. Bai, Formation of adiabatic shear band in metal matrix composites, *Int. J. Solids Struct.* 41 (22–23) (2004) 5979–5993.
- [67] L.H. Dai, L.F. Liu, Y.L. Bai, Effect of particle size on the formation of adiabatic shear band in particle reinforced metal matrix composites, *Mater. Lett.* 58 (11) (2004) 1773–1776.
- [68] D. Rittel, Z. Wang, M. Merzer, Adiabatic shear failure and dynamic stored energy of cold work, *Phys. Rev. Lett.* 96 (7) (2006) 075502.
- [69] Z.L. Tian, Y.J. Wang, Y. Chen, L.H. Dai, Strain gradient drives shear banding in metallic glasses, *Phys. Rev. B* 96 (9) (2017).
- [70] Z.Y. Yang, Y.J. Wang, L.H. Dai, Susceptibility of shear banding to chemical short-range order in metallic glasses, *Scr. Mater.* 162 (2019) 141–145.